OPEN ACCESS

REPORT

Radiation damage behavior of soft matter in ultrafast cryo-electron microscopy (cryo-UEM)

Yimin Zhao,[1,6] Chen Qi,[1,2,6] Chunhui Zhu,[2,3] Yun Zhu,[1,2] Yongzhao Zhang,[2,3] Tongnian Gu,[1,2] Huanfang Tian,[2,3] Wentao Wang,[2,3] Siyuan Huang,[2,3] Huaixin Yang,[2,3,*] Jianqi Li,[2,3,4,*] and Fei Sun[1,2,5,*]

*Correspondence: hxyang@iphy.ac.cn (H.Y.); ljq@aphy.iphy.ac.cn (J.L.); feisun@ibp.ac.cn (F.S.)

Received: June 21, 2025; Accepted: June 23, 2025; Published Online: July 2, 2025; https://doi.org/10.59717/j.xinn-life.2025.100145

© 2025 The Author(s). This is an open access article under the CC BY license (https://creativecommons.org/licenses/by/4.0/).

GRAPHICAL ABSTRACT

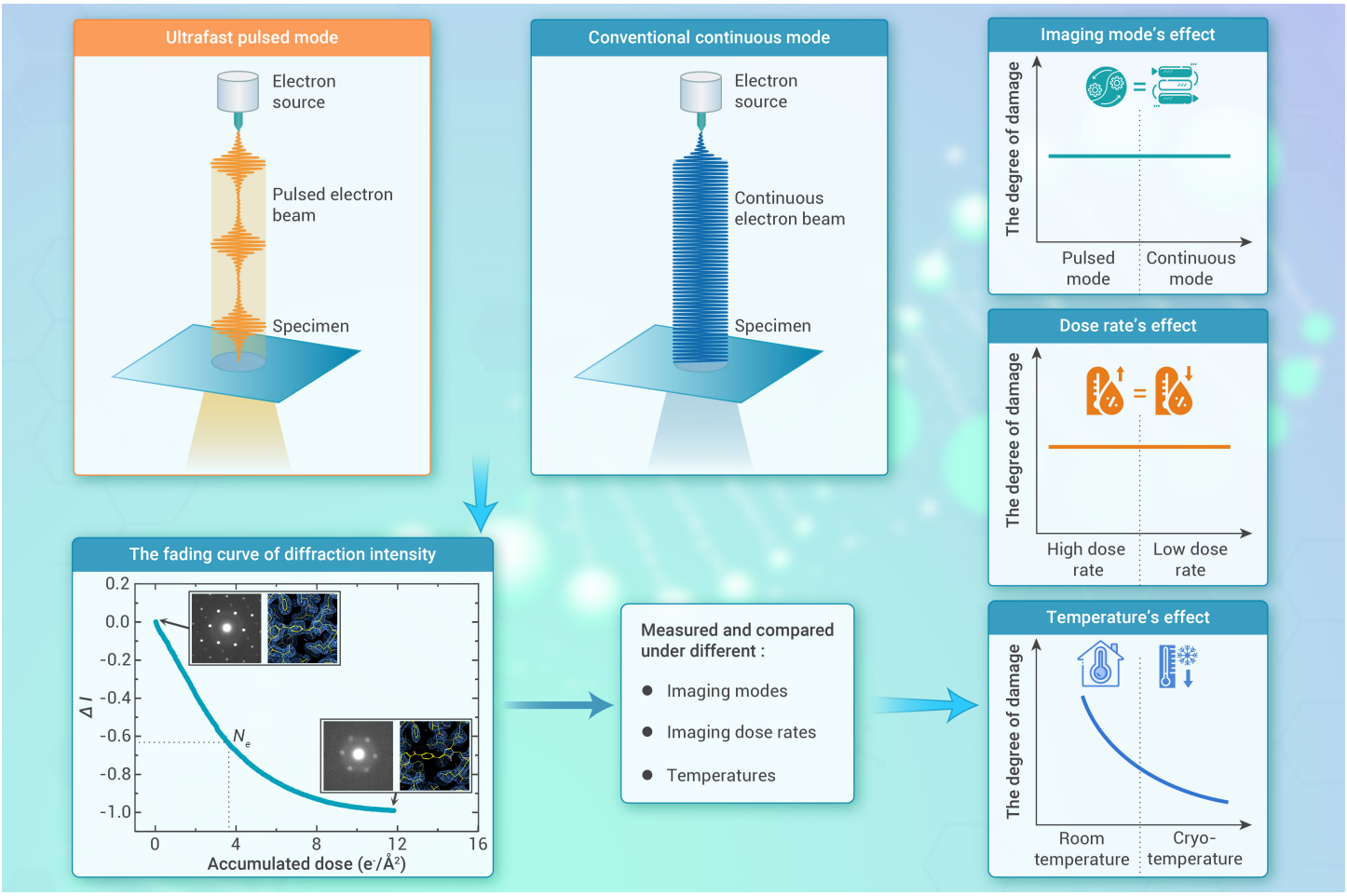

PUBLIC SUMMARY

- An ultrafast cryo-electron microscopy (cryo-UEM) system based on an ultrafast laser was established.
- Diffraction-intensity fading curves and critical doses of samples were measured under different conditions.
- The radiation damage in soft-matter samples did not show any dependence on the imaging electron dose rates.
- The pulsed electron beams cannot mitigate the radiation damage in room-temperature and cryogenic samples.
- The physical mechanisms behind the experimental results of radiation damage were systematically analyzed.

REPORT

OPEN ACCESS

www.the-innovation.org/life

Radiation damage behavior of soft matter in ultrafast cryo-electron microscopy (cryo-UEM)

Yimin Zhao,[1,6] Chen Qi,[1,2,6] Chunhui Zhu,[2,3] Yun Zhu,[1,2] Yongzhao Zhang,[2,3] Tongnian Gu,[1,2] Huanfang Tian,[2,3] Wentao Wang,[2,3] Siyuan Huang,[2,3] Huaixin Yang,[2,3,*] Jianqi Li,[2,3,4,*] and Fei Sun[1,2,5,*]

[1]National Key Laboratory of Biomacromolecules, CAS Center for Excellence in Biomacromolecules, Institute of Biophysics, Chinese Academy of Sciences, Beijing 100101, China
[2]University of Chinese Academy of Sciences, Beijing 100049, China
[3]Beijing National Laboratory for Condensed Matter Physics, Institute of Physics, Chinese Academy of Sciences, Beijing 100190, China
[4]Songshan Lake Materials Laboratory, Dongguan, Guangdong 523808, China
[5]Guangzhou Institutes of Biomedicine and Health, Chinese Academy of Sciences, Guangzhou 510530, China
[6]contributed equally to this work
*Correspondence: hxyang@iphy.ac.cn (H.Y.); ljq@aphy.iphy.ac.cn (J.L.); feisun@ibp.ac.cn (F.S.)

Received: June 21, 2025; Accepted: June 23, 2025; Published Online: July 2, 2025; https://doi.org/10.59717/j.xinn-life.2025.100145

© 2025 The Author(s). This is an open access article under the CC BY license (https://creativecommons.org/licenses/by/4.0/).

Citation: Zhao Y., Qi C., Zhu C., et al. (2025). Radiation damage behavior of soft matter in ultrafast cryo-electron microscopy (cryo-UEM). *The Innovation Life* **3**:100145.

Whether time-modulated pulsed-electron imaging can mitigate sample radiation damage is still controversial. The effectiveness of such mitigation and relevant potential applications in cryo-EM remain to be explored. Herein, we built an ultrafast cryo-EM system based on an ultrafast laser. Using such system and the saturated aliphatic hydrocarbon compounds ($C_{44}H_{90}$), the diffraction-intensity fading curves and corresponding critical electron doses (N_e) of samples were carefully measured under different imaging modes, temperatures, imaging dose rates and pulsed repetition rates. Our experimental results demonstrate that the fading curves and N_e values of $C_{44}H_{90}$ crystals show no correlation with the imaging electron dose rates. As the temperature decreased, the N_e values of the sample increased, indicating a cryoprotective effect on sample radiation damage. Interestingly, at constant temperature, the fading curves and N_e values of the sample in multi-electron-packet and near-single-electron-packet pulsed modes are all approximately the same as those in conventional continuous electron-beam mode, even when obtained at different pulsed repetition rates. These results show that the time-modulated pulsed electron beams do not appear to mitigate the electron radiation damage that occurs in samples. The physical mechanisms underlying the radiation damage behavior under different conditions were also carefully analyzed. Our findings provide new insights and an experimental basis for understanding sample radiation damage under electron beams, offering guidance and inspiration for elucidating the fundamental principles of radiation damage.

INTRODUCTION

Cryo-electron microscopy (Cryo-EM) has revolutionized the research progress in the field of life science through the "resolution revolution",[1-3] using methods such as sample cryoprotection[4,5] and low-electron-dose imaging[6,7] to mitigate the electron radiation damage during the imaging process. However, electron radiation damage is still the main factor limiting the further improvement of cryo-EM resolution, which is usually caused by electron-beam-induced atomic displacement and electronic excitation, and progressively triggers a series of cascading reactions leading to electrostatic charging, heating, radiolysis and diffusion events through inelastic electron-electron or electron-phonon scattering.[8,9] The factors and mechanisms associated with electron radiation damage are usually numerous and complex, with radiolysis originating from long-lived electronic excitation being the primary radiation damage mechanism for both organic and biological samples.[10-12] Cumulative ionization damage and bond-breaking limit the structural information that can be obtained before the sample is destroyed.[13] The ultimate bottleneck in cryo-EM technology is inevitably the physical nature of radiation damage to biomolecules during imaging, which is unavoidable by cryo-EM technology and limits the ability to achieve atomic resolution.[14-16]

Despite a relevant experiment having been reported recently,[17] whether ultrafast pulsed electron imaging can mitigate radiation damage in soft matter remains controversial.[12,18-20] Experiments by Flannigan *et al.* showed that the radiation damage of $C_{36}H_{74}$ crystals in ultrafast single-electron-packet pulsed mode was reduced by nearly 2 times, compared to continuous electron-beam mode at the same dose rates.[17] During radiation damage by cumulative ionization damage and bond-breaking, the excitation of each cascade reaction has its own characteristic temporal window.[21-23] Flannigan *et al.* believed that the segmented delivery of electrons using time-modulated pulses would allow sufficient relaxation time and sample recovery time for the cascade reaction and subsequent phonon excitation,[24,25] intercepting the occurrence of damage events and decreasing adverse synergistic or composite effects, thus reducing electron radiation damage to the sample to a certain extent. It should be noted that in their study,[17] the cumulative electron doses acting on the sample were very low (<0.1 $e^-/Å^2$), and the critical electron doses (N_e) of the sample were not obtained, which may be due to the long data collection time of pulsed electron imaging with the ultrafast laser-pulsed system. Glaeser *et al.* contested the validity of the claim that pulsed electron beams could mitigate sample radiation damage compared to conventional continuous beams (at the same electron dose rate).[20,26] They thought, to a first approximation, the average time between electrons could be arranged to be the same whether the electrons were emitted from the continuous sources or pulsed sources. As a result, simply reducing the intensity of a standard continuous electron source, rather than using an ultrafast pulsed source, should be much easier to provide a suitably long pause between individual inelastic scattering events for postulated thermal relaxation and "repair", implying that dose-rate effect should correlate with electron radiation damage to the sample. However, this was not the case in the experimental results of Glaeser *et al.*,[27,28] which showed that the dose-rate effect was independent of electron radiation damage.

Whether the dose rate correlates with radiation damage has also been debated for decades, and experimental results are controversial in both cryo-EM and X-ray crystallography.[18] Experiments supporting the view that radiation damage is independent of the dose rate found that, at the same total doses, lower dose rates were not conducive to high-resolution imaging,[27-32] where the fading of diffraction spots was only related to the total cumulative electron doses. Experiments supporting the opposite view suggested that there was dose-rate-dependent damage to the sample and that the critical dose was positively correlated with the dose rates.[33-35] Since the mechanism of radiation damage to samples is still not clear,[36] the correlation between radiation damage and dose rate remains to be explored.

With the progress of related technologies and methods, ultrafast electron microscopy (UEM) provides new opportunities to address the problem of conformational changes in biological samples.[37-41] The combination of UEM with cryo-EM not only enables ultrafast dynamic structural characterization of biomolecules on multiple time scales,[40,42-44] but also promises to be an effective means to explore the electron radiation damage behavior of low-temperature samples through ultrafast pulsed electron imaging modulated by time and electron number. On this basis, by modifying the hardware and software of conventional cryo-EM and introducing an ultrafast laser, we successfully built a biological ultrafast cryo-EM (cryo-UEM) system (Figure S1), and carried out a systematic study on whether the electron radiation damage of soft matter has time-modulated mitigation effect and dose-rate dependence.

Here, we use cryo-UEM to study the radiation damage behavior of $C_{44}H_{90}$

Table 1. Statistics and comparison of N_e values of $C_{44}H_{90}$ crystals obtained under different imaging conditions

Temperature (K)	Imaging mode	Imaging dose rate ($e^-/Å^2/s$)	Critical electron doses (N_e) ($e^-/Å^2$)
300	Continuous electron-beam mode	6.72×10^{-5} – 1.00×10^{-2}	3.6 ± 0.1
	200 kHz pulsed electron-beam mode	Multi-electron per pulsed packet	3.62
		Near single electron per pulsed packet	3.67
	100 kHz pulsed electron-beam mode	Multi-electron per pulsed packet	3.62
		Near single electron per pulsed packet	3.58
200	Continuous electron-beam mode	8.23×10^{-5} – 5.28×10^{-3}	5.8 ± 0.1
	200 kHz pulsed electron-beam mode	Multi-electron per pulsed packet	5.76
		Near single electron per pulsed packet	5.85
140	Continuous electron-beam mode	8.23×10^{-5} – 1.89×10^{-2}	9.8 ± 0.1
	200 kHz pulsed electron-beam mode	Multi-electron per pulsed packet	9.62
		Near single electron per pulsed packet	10.04

crystals at different temperatures and imaging modes. By overcoming problems such as electron-dose fading and by collecting experimental data over long periods, continuously and repeatedly, we obtained the diffraction-intensity fading curves and N_e values of the samples at high cumulative electron doses under different imaging conditions (Table 1). Comparative analysis showed that the fading curves and N_e values of $C_{44}H_{90}$ crystals do not change at different imaging electron dose rates, indicating that their radiation damage does not exhibit a dependence on the dose-rate effect. Under constant temperature, the fading curves and N_e values of $C_{44}H_{90}$ crystals are essentially the same in both conventional continuous and ultrafast pulsed modes. We found that, different from the recent report,[17] time-modulated pulsed electron beams do not seem to mitigate the electron radiation damage to our samples.

MATERIALS AND METHODS

Sample preparation

Preparation method for saturated aliphatic hydrocarbon ($C_{44}H_{90}$) samples: the Cu grids loaded with carbon films (300 mesh, Beijing Zhongjingkeyi Technology Co., Ltd, the thickness of carbon films: ~10 nm) were treated with glow discharge (O_2, Ar) for 60 s using a glow discharger (Gatan SOLARUS 950). Subsequently, 3 μL of the supernatant of a saturated solution of $C_{44}H_{90}$ in *n*-hexane was dropped onto the grids and allowed to dry in air. As a result, the rhombic $C_{44}H_{90}$ monocrystals oriented along the [001] crystallographic direction and dispersed on the grids were obtained. These crystals had low intrinsic defect density and uniform monomolecular-layer thickness.[13,45,46]

Data collection

All experiments (conventional continuous and ultrafast pulsed modes) were performed on a 200-kV JEM-2100Plus cryo-transmission electron microscope (JEOL) equipped with a Gatan OneView CMOS detector. The JEM-2100Plus was equipped with a LaB_6 thermic cathode and Wehnelt cylinder. To generate discrete pulsed electron packets through laser-driven (*i.e.*, unheated) emission, an additional vacuum chamber together with optical components was integrated into the TEM column near the anode for optical access to the LaB_6 cathode.[47] Ultrafast laser pulses at a center wavelength of 1030 nm were generated by a Yb-based laser amplifier (Carbide 5W, Light Conversion Inc.), with a pulse duration ≤ 300 fs and a maximum average power of up to 5 W. The laser output was split into two pulses using a beam splitter. One pulse, for driving photoemission (probe), was focused on the TEM cathode after being converted to 257 nm by fourth-harmonic generation using beta barium borate (BBO) crystals. Diffraction patterns under different temperatures and modes were recorded on a Gatan OneView CMOS detector using a camera length of 50 cm. The diameter of the illuminated area was 5 μm (circled by the selected-area aperture), and before data collection, a careful check was made to ensure that the electron beams were fully irradiated on the crystal areas. Diffraction patterns were automatically saved using custom Matlab scripts. For both ultrafast pulsed mode and low-dose-rate (≤ 10^{-5} $e^-/Å^2/s$) continuous mode, the exposure time of each diffraction-pattern image was 180 s. For data collection at higher dose rates (≥ 10^{-4} $e^-/Å^2/s$) in continuous mode, the exposure time per diffraction-pattern image decreased accordingly: 60 s at a dose rate of 10^{-4} $e^-/Å^2/s$, 20 s at 10^{-3} $e^-/Å^2/s$, and 10 s at 10^{-2} $e^-/Å^2/s$, with a 5-s interval between images. *Gatan Digital Micrograph* and *Python* software were used for data collection and analysis, respectively (Script S1). Analysis of a set of data was performed by measuring the intensity of four diffraction spots of the {110} index.

Detector reading saturation and intensity drift of dark current images: Problems and solutions

When diffraction imaging is performed on the crystal in the focal plane, the focused central transmission spot and diffraction spots will appear very sharp. The intensities of these spots will be mainly concentrated in a few or even one pixel on the detector, which may lead to saturation of the detector, resulting in the recorded electron intensity being lower than the true value (Figure S2). To solve this problem, we developed the following strategy: A sample area on the TEM grid was selected for a pre-experiment. First, a real-space image was acquired with a fixed exposure time in real-space imaging mode, from which the total electron intensity incident on the sample was measured (Figure S2A). Then the imaging mode was switched to diffraction and a diffraction pattern was taken with the same experimental parameters. When no detector saturation occurred, the total electron intensity in the diffraction pattern should be the same as that in the real-space image. However, the detector saturation events (caused by the focused central transmission spot and diffraction spots) resulted in the electron intensity recorded in the diffraction pattern being lower than that recorded in the real-space image (Figure S2B). In this case, the diffraction pattern could be moved away from the focal plane by changing the defocus values, so that the central transmission spot and diffraction spots were slightly diffused, causing their intensity to be borne by more pixels on the detector, thereby reducing the occurrence of reading saturation events (Figure S2C). By incrementally increasing the defocus values, a condition where the total electron intensity in the diffraction pattern matched that of the real-space image could be identified (indicating negligible saturation) (Figure S2D). Further defocusing beyond this optimal range was avoided, as it degraded the sharpness of diffraction spots and complicated intensity quantification during data processing (Figures S2E-F). This approach, analogous to methods described in Ref.[45], allowed us to establish defocus conditions suitable for reliable diffraction data collection. Note that diffraction intensities needed to be carefully screened before data collection was performed. We found that even in the pulsed imaging mode (less coherent than the continuous electron-beam mode) with a very low dose rate, saturation of the detector readings would occur if not handled properly.

An unexpected problem was that during the experiment, we found that the intensity of the dark current images taken by the detector, in the absence of electron radiation, did not remain stable near zero, but slowly drifted towards

negative values over time (Figure S3A). Since the dark current image was taken to subtract background noise after completing sample data collection (by default, the intensity of the dark current image remained constant throughout the collection process), such drift effect would make the intensity value of the sample image obtained too high, ultimately resulting in an overestimated cumulative electron dose. To address this problem, we developed the following strategy: Before data collection, the detector was first used to continuously record images in the open holes on carbon film, and dark current images with the shutter turned off were recorded at 5-hour intervals. When drift was observed to occur, the intensity of the dark current image was corrected once by the *Gatan Digital Micrograph* (*GMS*) software. After approximately 30 hours of this correction cycle, the intensity of the dark current image would be observed to stabilize around the zero value without any drifting (Figure S3B).

The effect of background scattering on crystal diffraction intensity: Estimation and correction

Before statistical analysis of the diffraction intensity data, the background scattering noise in the diffraction intensity values was estimated and corrected. A thorough evaluation of the potential impact of background scattering (*e.g.*, scattering from the support film) on the experimental results was conducted (Figure S4): Under the same imaging conditions, three diffraction patterns were acquired from the sample area, the pure support-carbon-film area, and the open-hole area, respectively. By referencing the position of the crystal {110} diffraction spots, the electron intensities of corresponding regions across the three patterns (marked by green lines in Figures S4A-C) were compared and analyzed. We noticed that compared to the open-hole area, the support carbon film did contribute excess electron intensities at the location where the diffraction spots appeared under the influence of background scattering (the intensity in open-hole area: 6.08×10^3; the intensity in carbon-film area: 1.82×10^5). Compared with the sample, the statistical value of electron intensity caused by the carbon support film was relatively minor (1.37×10^7 *vs.* 1.82×10^5), accounting for about 1.33% of the crystal diffraction intensity.

To correct the crystal diffraction intensity by subtracting background scattering contributions, we implemented the following procedure: First, two regions centered on the crystal {110} diffraction spot were marked (Figures S4D-E). One marked region (green) precisely encompassed the diffraction spot area, while the other marked region (orange) covered a larger area (approximately four times larger) to delineate the background surrounding the diffraction spot. Subsequently, a script was developed to extract the diffraction intensity value from the small marked region (green) (*value* A). Next, the average electron intensity within the larger marked region (orange), excluding the small marked area, was calculated *via* the script (Figure S5). Such average intensity represented the contribution of background scattering at the diffraction spot. The average intensity value was then multiplied by the area of the small marked region to determine the electron-intensity contribution from background scattering at the diffraction-spot region (*value* B). Finally, the corrected diffraction intensity was obtained by subtracting *value* B from *value* A (Figure S4F). We described the data processing methods used in the statistical analysis of diffraction intensities (Script S1), and the *ND_spotI.py* script mentioned in the description contained the specific algorithm for background scatter correction (Figure S5).

The solution to dose-rate fading problem in ultrafast pulsed electron-beam mode

Data collection of fading curves in ultrafast pulsed mode usually requires a long time, which places demands on the stability of the pulsed electron beams. The addition of ultrafast laser systems not only affects the vacuum level of the TEM system, but also makes the pulsed electron beams particularly sensitive to environmental conditions. To convert the thermally excited continuous electron beams into laser-excited pulsed electron beams, the heating current of the TEM filament also needs to be reduced, which induces a decrease in the filament temperature. The decrease in TEM-vacuum level and filament temperature in ultrafast pulsed mode will lead to the gradual adsorption of impurities on the filament, hindering electron excitation at the filament tip. We noted that during data collection in ultrafast pulsed mode, the number of electrons in each pulse decreased quickly (Figure S6A), causing a rapid decrease in the electron dose rates and ultimately losing the ability to perform diffraction imaging of the sample (Figure S6B). To solve the fading problem of electron dose rates, we applied a "photoexcitation-thermal excitation-photoexcitation" experimental strategy when the electron dose rates in pulsed mode were too low: In the ultrafast pulsed mode of photoexcitation, when a significant reduction in electron-beam intensity was observed, the data collection was paused and the laser pulse was switched off to exit the photoexcitation mode. Then the shutter on the sample holder was turned off to protect the sample and the heating current of the filament was increased back to thermal excitation mode to burn off impurities adsorbed on the filament for two minutes (without changing the sample position or other parameters of the TEM). Finally, the heating current of the filament was reduced to the level used for photoexcitation mode, the laser pulse and shutter were turned on, and data collection was continued. Here, the heating of thermal excitation was used to clean the filament and increase the electron dose rates in pulsed mode (electrons/pulse). The repeated adoption of this strategy during the experiment could effectively enhance the electron dose rates of pulsed electron beams and successfully allow us to obtain the fading curves of diffraction intensity in the ultrafast pulsed mode (Figures S6C-D & S7).

The above strategy still had some new problems: the electron dose rates needed to be adjusted manually frequently to maintain the collection of experimental data (Figure S7), which would greatly increase the data collection time. To improve the vacuum environment in the filament area and mitigate impurity adsorption on the filament, we added a new ion pump near the filament area (Figure S8). During the subsequent experiments, we observed that the fading of pulsed-electron dose rates was effectively mitigated after the addition of the ion pump (Figure S9), although occasional manual adjustments were still required.

Measurement of the minimum tolerable temperature for TEM system

The impurities in the TEM chamber were not only adsorbed on the filament, but may also be adsorbed on samples at low temperatures, which required determining the minimum tolerable temperature at which the vacuum in the TEM chamber did not affect the sample. After lowering the temperature of the samples in the TEM chamber from 300 K to 100 K and leaving for a period of time, the samples at 100 K exhibited spontaneous fading of diffraction spots, the appearance of new amorphous rings and the disappearance of morphological information, indicating the adsorption and condensation of impurities on the samples (Figure S10).

To investigate the minimum tolerable temperature at which the current vacuum in the TEM chamber did not affect the sample, a new experimental strategy was devised in which the incident electron intensity (I_{in}) was collected in the open holes in real-space imaging mode, followed by the transmitted electron intensity (I_{out}) on the sample in diffraction imaging mode. It should be noted that imaging the focused diffraction pattern here (the spots appeared very sharp) would saturate the detector readings, thus affecting the ratio of incident and transmitted electron intensity (I_{in}/I_{out}). At a constant incident electron intensity (I_{in}), the saturation value of detector readings would only show a strong sensitivity to the state of samples, and could thus be used to monitor whether impurity adsorption and condensation occurred on the samples, which was ultimately manifested by a change in the I_{in}/I_{out} ratio. By measuring the change in the I_{in}/I_{out} ratios of samples at different temperatures over time while held in the chamber, it could be determined whether they were affected by impurities in the chamber, and thus determine the minimum temperature tolerable for the TEM chamber vacuum. Our experimental results showed that the I_{in}/I_{out} ratios changed over time at temperatures between 100 K and 135 K. However, at 140 K and above, the I_{in}/I_{out} ratios remained stable with the extension of placement time, indicating that the minimum tolerable temperature for the TEM vacuum was about 140 K (Figure S11).

Measurement of electron dose rates in ultrafast pulsed mode

The instability of the electron beams in ultrafast pulsed mode also made it difficult to obtain the electron doses acting on each image. Here we used Beer-Lambert's law[48,49] to calculate the electron dose rates acting on the last

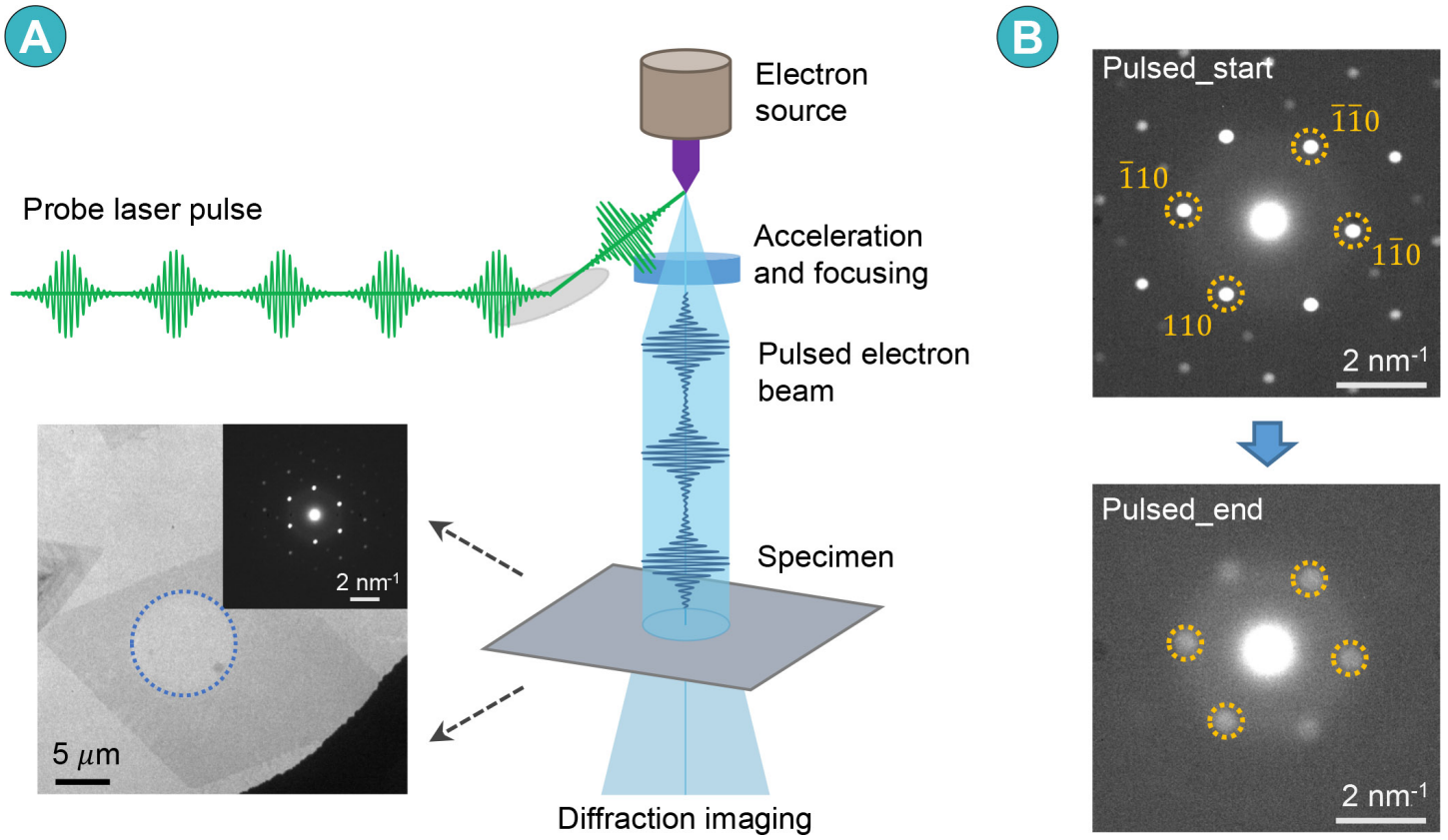

Figure 1. Experimental procedures for ultrafast pulsed electron imaging on $C_{44}H_{90}$ crystals. (A) Schematic diagram of pulsed electron imaging driven by an ultrafast laser system, with the radiated region on the rhombic crystal marked by the blue dashed lines in the lower-left inset. The real-space image and diffraction pattern of the crystal were obtained in the conventional continuous electron-beam mode at 300 K. (B) Diffraction patterns of $C_{44}H_{90}$ crystals obtained in the ultrafast pulsed mode, with the four diffraction points of {110} index used for the statistics of diffraction intensity marked by orange dashed lines. These diffraction patterns were obtained in the 200 kHz ultrafast pulsed electron-beam mode at 300 K.

image:

$$I_{in} = I_{out} \times e^{\frac{d_e}{\lambda_{in}}} \quad (1)$$

where I_{in} was the incident electron intensity, I_{out} was the transmitted electron intensity, d_e was the effective thickness of the sample, λ_{in} was the mean free path for inelastic electron scattering.

After completing the collection of the last image (from which the transmitted electron intensity (I_{pulsed_out}) could be obtained) in ultrafast pulsed mode, the shutter was turned off to protect the sample, followed by switching off the laser pulse and increasing the heating current of filament back to conventional continuous (thermal excitation) mode and allowing it to stabilize for half an hour. During this process, the sample position was not moved and other parameters of the TEM were not changed. A diffraction pattern and a dark current image of the sample were taken in the conventional continuous mode, from which the transmitted electron intensity ($I_{continuous\_out}$) was obtained (defocused to prevent detector saturation). The electron beams were then immediately moved to the open-hole area, a blank image and a dark current image were taken in real-space imaging mode, from which the incident electron intensity ($I_{continuous\_in}$) was obtained. According to Beer-Lambert's law, for the same sample and the same electron acceleration voltage (200 kV), the ratios of incident and transmitted electron intensities in continuous and pulsed modes should be the same:

$$\frac{I_{continuous\_in}}{I_{continuous\_out}} = e^{\frac{d_e}{\lambda_{in}}} = \frac{I_{pulsed\_in}}{I_{pulsed\_out}} \quad (2)$$

where $I_{continuous\_in}$ and $I_{continuous\_out}$ were the incident and transmitted electron intensities in conventional continuous mode, respectively. I_{pulsed_in} and $I_{pulseds\_out}$ were the incident and transmitted electron intensities in ultrafast pulsed mode, respectively.

Therefore, according to the ratio of $I_{continuous\_in}/I_{continuous\_out}$ and the value of I_{pulsed_out}, the incident electron intensity of the last image in ultrafast pulsed mode (I_{pulsed_in}) was obtained. Based on the ratios of the electron intensity of the latter image to that of the former image, the corresponding electron dose rates for all images could be obtained sequentially:

$$I_{pulsed\_in\_n-1} = I_{pulsed\_out\_n-1} \times \frac{I_{pulsed\_in\_n}}{I_{pulsed\_out\_n}} \quad (3)$$

$$I_{pulsed\_in\_n-2} = I_{pulsed\_out\_n-2} \times \frac{I_{pulsed\_in\_n-1}}{I_{pulsed\_out\_n-1}} \quad (4)$$

.....

.....

$$I_{pulsed\_in\_1} = I_{pulsed\_out\_1} \times \frac{I_{pulsed\_in\_2}}{I_{pulsed\_out\_2}} \quad (5)$$

where $I_{pulsed\_in\_n}$ and $I_{pulsed\_out\_n}$ were the incident and transmitted electron intensities of the last image in ultrafast pulsed mode; $I_{pulsed\_in\_n-1}$ and $I_{pulsed\_out\_n-1}$ were the incident and transmitted electron intensities of the second to last image in ultrafast pulsed mode; $I_{pulsed\_in\_n-2}$ and $I_{pulsed\_out\_n-2}$ were the incident and transmitted electron intensities of the third to last image in ultrafast pulsed mode; $I_{pulsed\_in\_2}$ and $I_{pulsed\_out\_2}$ were the incident and transmitted electron intensities of the second image in ultrafast pulsed mode; $I_{pulsed\_in\_1}$ and $I_{pulsed\_out\_1}$ were the incident and transmitted electron intensities of the first image in ultrafast pulsed mode.

Finally, based on the conversion constant (37) between the imaging contrast and electron counts of the detector we used, the electron dose rates acting on the different images could be obtained. To facilitate the calculations, we wrote the scripts using *Python* for corresponding data processing (Script S1).

The feasibility of the newly established data-processing method was first verified by using the experimental data obtained in the conventional continu-

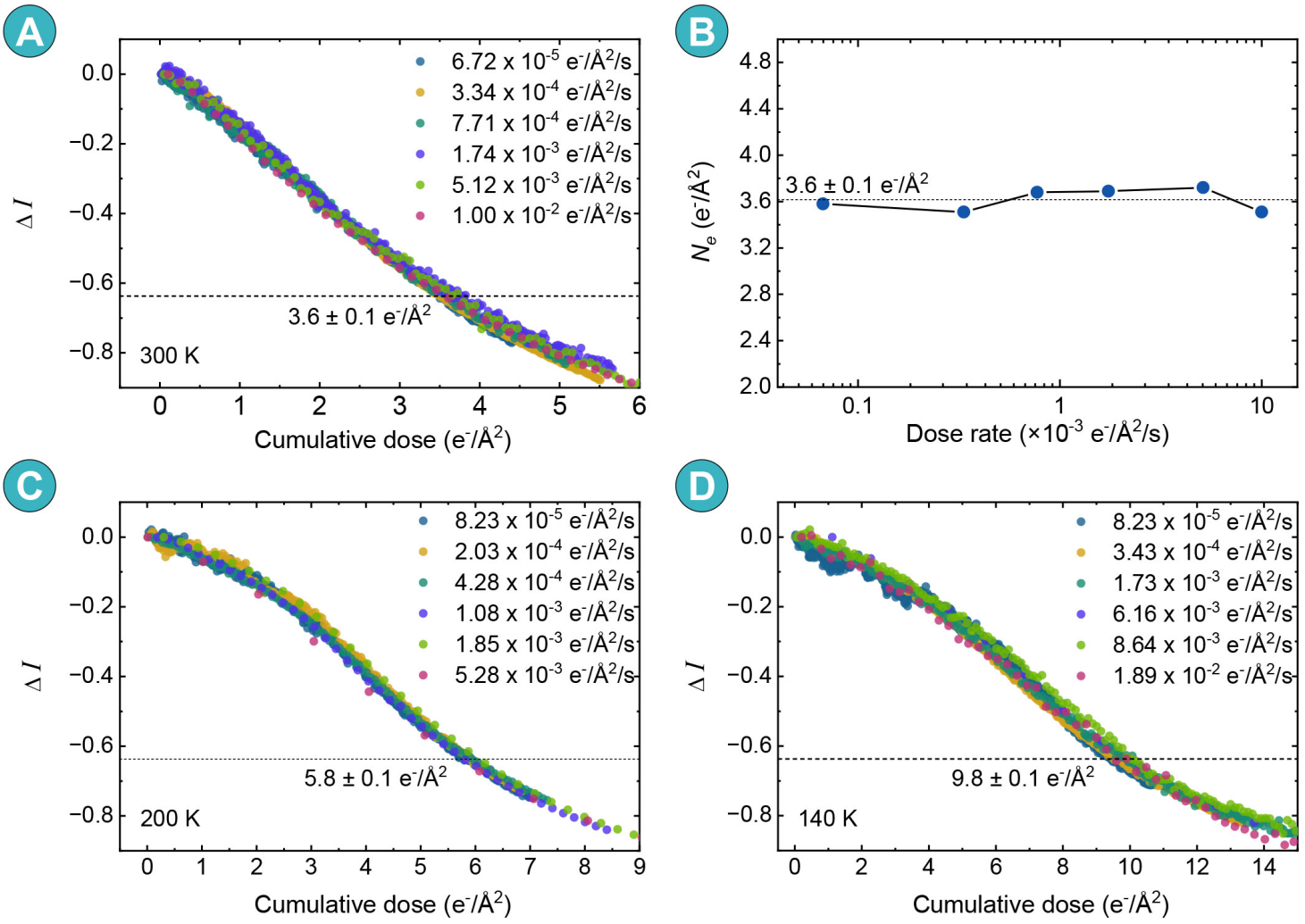

Figure 2. Electron radiation damage of $C_{44}H_{90}$ crystals in conventional continuous electron-beam mode and at different temperatures (300 K, 200 K and 140 K) (A) The fading curves of diffraction intensity on $C_{44}H_{90}$ crystals measured at different electron dose rates at 300 K, which showed that the fading rate is independent of dose rate. (B) N_e values obtained from the fading curves under different electron dose rates in (A). The N_e values do not change with increasing electron dose rates and have a value of 3.6 ± 0.1 $e^-/Å^2$ within the random error (standard deviation). (C-D) The fading curves of diffraction intensity measured at different dose rates at 200 K (C) and 140 K (D), with corresponding N_e values of 5.8 ± 0.1 $e^-/Å^2$ and 9.8 ± 0.1 $e^-/Å^2$, respectively. The N_e values extracted from different fading curves in the figure, along with the average N_e values and standard deviations obtained under each temperature, were systematically summarized in Table S1.

ous electron-beam mode. The diffraction-intensity fading curves and N_e values obtained by the newly established data-processing method were the same as those obtained by directly reading the electron dose rates, which proved the validity of the above data processing method based on Beer-Lambert's law. For consistency, the data processing of continuous mode also used the same method based on Beer-Lambert's law as the pulsed mode.

RESULTS

The development of biological cryo-UEM and experimental scheme

A 200-kV biological cryo-UEM system with picosecond stroboscopic and nanosecond single-pulse electron mode was developed, which was mainly composed of an ultrafast laser system and a biological cryo-EM system integrated after modification (Figure S1). The key points of this new cryo-UEM system included the modification of the cryo-EM electron source and sample chamber, the precise introduction of the ultrafast laser, the co-axis adjustment in the pulsed mode, the search for the time-zero and ultrafast signals, the precise monitoring and adjustment of the laser position, and the installation and debugging of the direct electron detector. The cryo-UEM could be used to study the ultrafast dynamic conformational changes of photosensitive proteins. Here, it is mainly used to study the radiation damage behavior of soft matter represented by saturated hydrocarbon crystals ($C_{44}H_{90}$) (Text S1) under time-modulated pulsed electron beams.

$C_{44}H_{90}$ monocrystals were prepared using the drop-casting method, formed flat layers on carbon films, and had a single-molecule-layer thickness with a rhombic morphology (Figure 1). Diffraction patterns were intentionally defocused to prevent detector saturation.[45] A dark current image for the correction of diffraction intensity was taken by masking the sample with shutter after each set of data was collected in both conventional continuous and ultrafast pulsed modes. The fading curves and N_e values for the $C_{44}H_{90}$ {110} diffraction spots under electron radiation were statistically analyzed (Figure 1). The N_e (critical electron dose) is defined as the cumulative electron dose at which the diffraction intensity of the sample at given resolution fades to *1/e* (~37%) of the initial value.[50,51] This dose determines the maximum electron dose that the sample can withstand without significant structural degradation (at the given resolution). As a standardized parameter, the N_e has been widely adopted for comparative assessment of radiation damage susceptibility across imaging modalities. For detailed definitions and methodological explanations, see Text S2.

During the experiments, various problems such as the saturation of detector readings, the intensity drift of dark current images, the instability of pulsed electron beams, and the temperature intolerance of samples in the cryo-UEM system, brought difficulties to our experimental progress. The saturation of detector readings was mainly caused by the focused central transmission spot and diffraction spots being too "sharp", resulting in the intensity of these areas exceeding the detector reading range. This issue was solved by testing the defocus conditions required for the detector reading to be unsaturated before data collection (Figure S2). The intensity drift of dark current images meant that the intensity of dark current images (acquired without electron

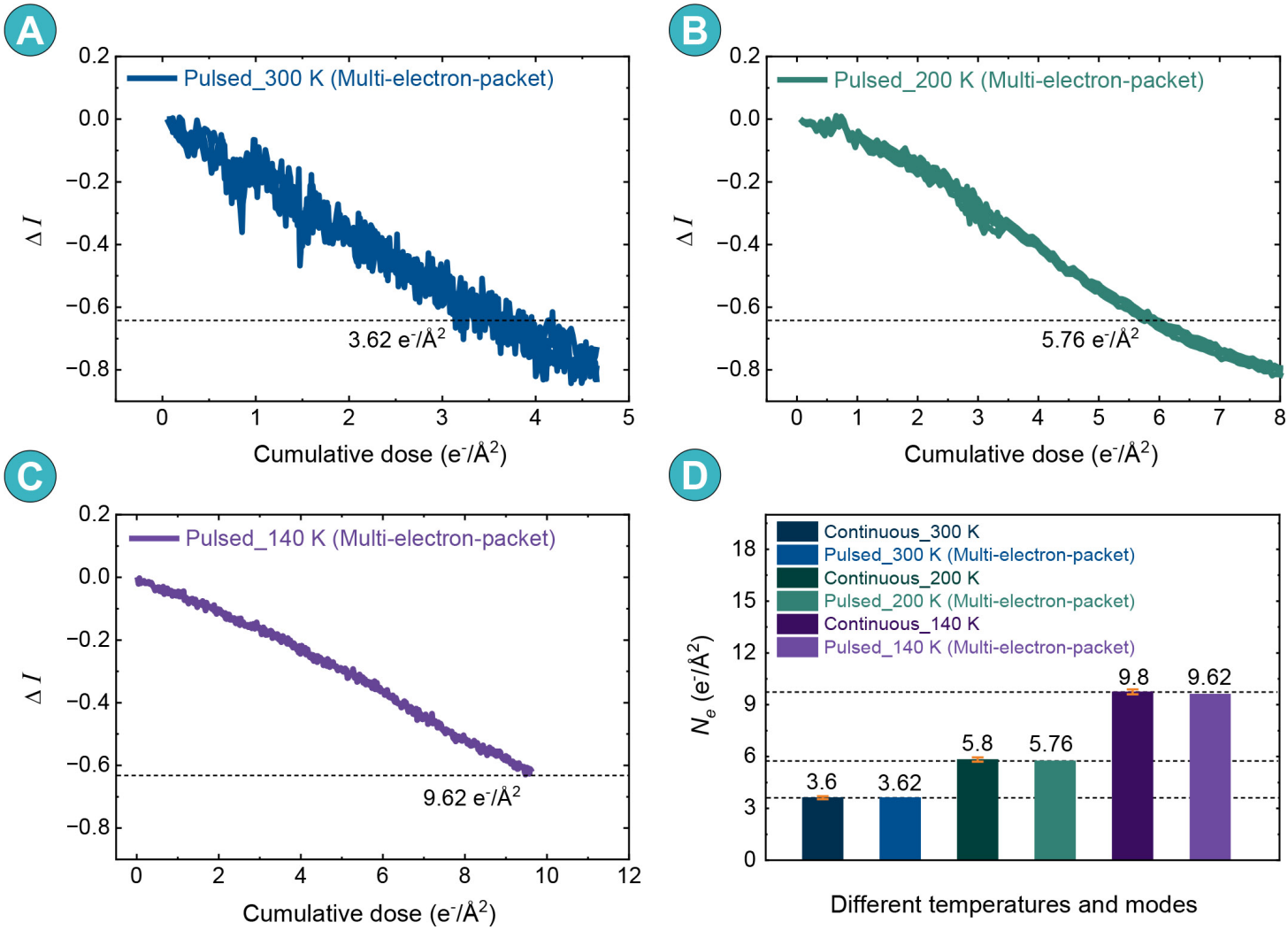

Figure 3. Electron radiation damage of $C_{44}H_{90}$ crystals in ultrafast multi-electron-packet pulsed electron-beam mode at different temperatures (A-C) The fading curves of diffraction intensity in ultrafast multi-electron-packet pulsed mode at 300 K (A), 200 K (B) and 140 K (C), with N_e values of 3.62 $e^-/Å^2$, 5.76 $e^-/Å^2$ and 9.62 $e^-/Å^2$. (D) N_e-value statistics of $C_{44}H_{90}$ crystals obtained in multi-electron-packet pulsed mode and conventional continuous electron-beam mode at different temperatures, among which the N_e values in the continuous mode were derived from the average and standard deviation in Figure 2.

radiation) did not stabilize around zero but slowly drifted towards negative values over time. This was addressed by performing multiple corrections on the dark current image for its drift over time before data acquisition (Figure S3). Moreover, to avoid noise interference from background scattering near the diffraction spots, background signal correction was also implemented (Figures S4-S5). The instability of the pulsed electron beams presented two significant challenges: First, during pulsed data acquisition, the intensity of the laser-excited pulsed electron beams would fade rapidly, losing the ability to perform diffraction imaging of the sample. This issue was resolved through the installation of an additional ion pump near the filament area and the adoption of a manually adjusted "photoexcitation-thermal excitation-photoexcitation" experimental strategy (Figures S6-9). Second, the instability of pulsed electron beams also made it impossible to directly read the electron dose acting on each image. To address this, we designed an experimental and calculation method that used Beer-Lambert's law[48,49] to obtain the average electron dose rate acting on the last image, and iterated forward in sequence to obtain the electron dose of all images. During the experiment, we also noticed that the degraded vacuum level in the modified cryo-UEM system led to an intolerance of samples being held in the cryo-UEM chamber to the low temperature of 100 K (Figure S10). By establishing a monitoring method for the state of samples at different temperatures in cryo-UEM, we finally confirmed that the lowest tolerable temperature for samples within the cryo-UEM chamber was about 140 K (Figure S11). See the Materials and Methods section for details.

Radiation damage behavior of $C_{44}H_{90}$ crystals in conventional continuous electron-beam mode

The diffraction-intensity fading curves of $C_{44}H_{90}$ crystals were first measured at room temperature (300 K) and in conventional continuous electron-beam mode (200 kV) (Figures 2A & S12). The imaging electron dose rates were controlled by modulating the cryo-UEM filament current. After each adjustment, a stabilization period was necessary to ensure the equipment reached a steady state, and data collection commenced upon confirmation of the stable imaging electron dose rates. Experimental results revealed that across a range of imaging electron dose rates (6.72×10^{-5} to 1.00×10^{-2} $e^-/Å^2/s$), the diffraction-intensity fading curves of the $C_{44}H_{90}$ crystals were all essentially the same, exhibiting consistent decreasing trends and curve slopes. The N_e values obtained from the fading curves of diffraction intensity at different dose rates were also statistically analyzed, and as shown in Figure 2B and Table S1, the N_e values did not exhibit a correlation with the electron dose rates, but remained constant at a value of 3.6 ± 0.1 $e^-/Å^2$ in the conventional continuous electron-beam mode at 300 K.

Furthermore, low-temperature experiments were also conducted. Despite the increased experimental complexity, the related experiments have the following advantages: they enable both a lateral analysis of the diffraction-intensity fading curves and the N_e values of samples across different modes at the same temperature, as well as a longitudinal analysis of these parameters in the same mode at different temperatures. This can not only investigate the impact of temperature on the sample radiation damage under various modes, but also provide supporting evidence for the existence or non-

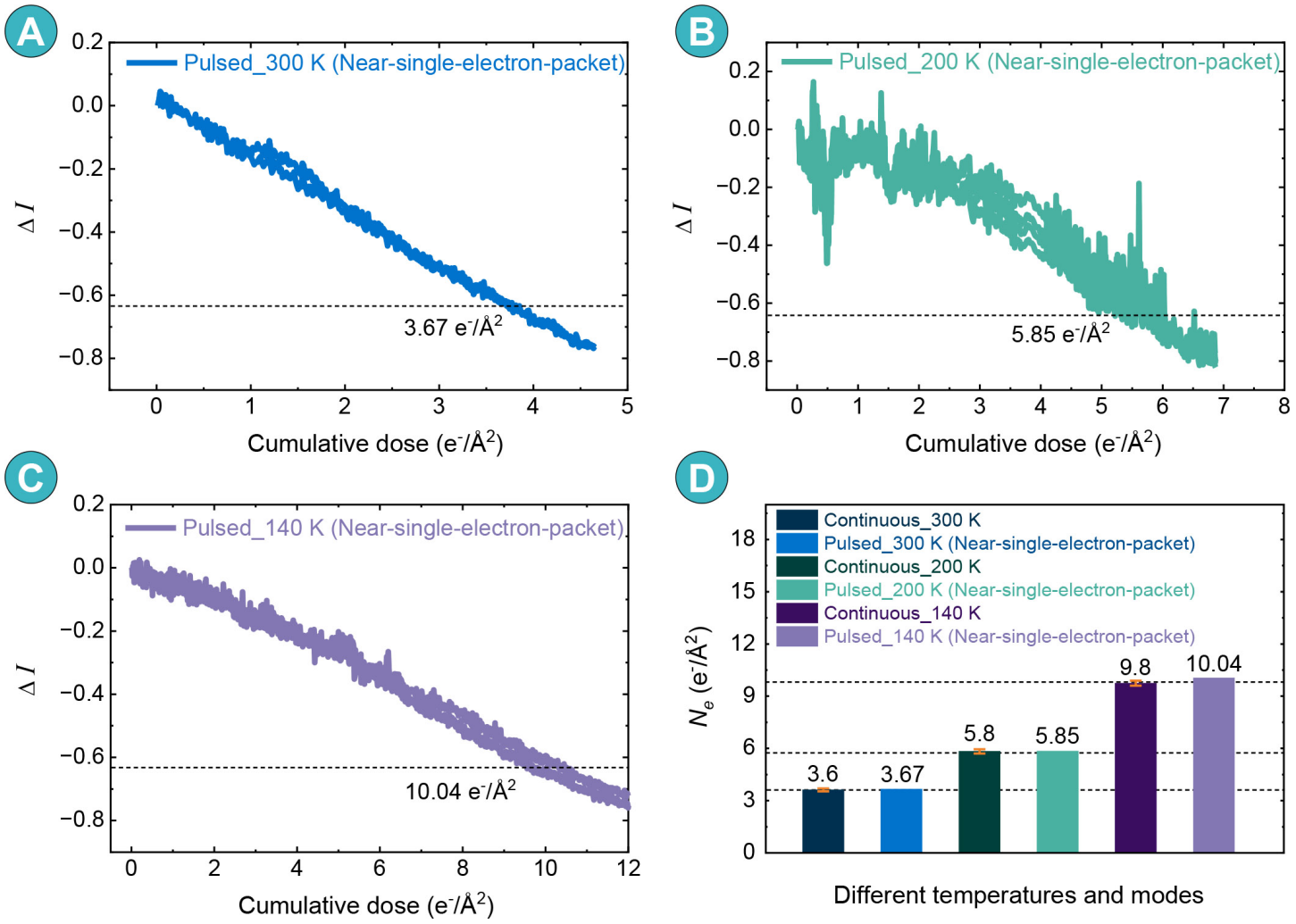

Figure 4. Electron radiation damage of $C_{44}H_{90}$ crystals in ultrafast near-single-electron-packet pulsed electron-beam mode at different temperatures (A-C) The fading curves of diffraction intensity in ultrafast near-single-electron-packet pulsed mode at 300 K (A), 200 K (B) and 140 K (C), with N_e values of 3.67 $e^-/Å^2$, 5.85 $e^-/Å^2$ and 10.04 $e^-/Å^2$. (D) N_e-value statistics of $C_{44}H_{90}$ crystals obtained in near-single-electron-packet pulsed mode and conventional continuous electron-beam mode at different temperatures, among which the N_e values in the continuous mode were derived from the average and standard deviation in Figure 2.

existence of radiation-damage mitigation effect in the ultrafast pulsed mode. At different electron dose rates in the range of 8.23×10^{-5} – 5.28×10^{-3} $e^-/Å^2/s$ and 8.23×10^{-5} – 1.89×10^{-2} $e^-/Å^2/s$, the diffraction-intensity fading curves of $C_{44}H_{90}$ crystals in the conventional continuous mode were measured at 200 K and 140 K, respectively (Figures 2C-D). The experimental results showed that the diffraction-intensity fading curves of $C_{44}H_{90}$ crystals at different electron dose rates were also essentially the same at 200 K, showing the same decreasing trends and corresponding to an N_e value of 5.8 ± 0.1 $e^-/Å^2$. The fading curves of diffraction intensity, which were not correlated to the electron dose rates, were also observed at 140 K, corresponding to a N_e value of 9.8 ± 0.1 $e^-/Å^2$ (Table S1). These experimental results demonstrate that the radiation damage of $C_{44}H_{90}$ crystals under the electron beams exhibits no dependence on the imaging electron dose rates, but only a correlation with the cumulative electron doses.

Moreover, compared to those at 300 K, the corresponding N_e values of $C_{44}H_{90}$ crystals at 200 K and 140 K were increased by about 1.61 (5.8 *vs.* 3.6) and 2.72 times (9.8 *vs.* 3.6), respectively (Figure 2 & Table 1), indicating the mitigation effect of radiation damage in the samples at low temperatures. In addition, we found that the fading curves of diffraction intensity at 200 K and 140 K showed a "first slow then fast" fading compared to those at 300 K. We attributed the "first slow then fast" two-stage form of fading curves to the "latent dose" effect[5,52] exhibited by the samples at low temperatures: at low temperatures, the molecular fragments were "frozen" and their diffusion rates were suppressed. Only after reaching the latent dose, the stress generated in the crystals, due to the increasing number of fragments, would lead to the acceleration of the diffusion of the fragments (due to the cage effect,[53] the molecular-diffusion rates were still lower than the rates at room temperature), resulting in a gradual fading of the diffraction intensity. We believed that the mitigation effect of radiation damage at low temperatures was produced synergistically by the presence of latent dose and the decrease in the diffusion rates of molecular fragments.

Radiation damage behavior of $C_{44}H_{90}$ crystals in ultrafast pulsed electron-beam mode (200 kHz)

Using the newly established experimental strategy and data processing method (Materials and Methods section), the diffraction-intensity fading curves of $C_{44}H_{90}$ crystals in ultrafast pulsed electron-beam mode (laser repetition rate of 200 kHz) and in the temperature range of 140 – 300 K were measured. The temporal modulation of the imaging electron beams by 200 kHz probe laser resulted in a 5 μs time interval between successive pulsed electron packets, to allow for the possible potential ground-state recovery and structural relaxation of samples. Figure 3 shows the experimental results measured in the ultrafast multi-electron-packet pulsed mode, where the number of electrons in each pulsed electron packet fluctuated between 1 and 8. More than three sets of data for each mode were measured independently and compared with the experimental results in the conventional continuous electron-beam mode (Figure S13). It can be found that the diffraction-intensity fading curves obtained at room temperature (300 K) were essentially the same for the multi-electron-packet pulsed mode and the conventional continuous mode. At 200 K and 140 K, similar results to those in the conventional continuous mode were also observed in the ultrafast multi-electron-

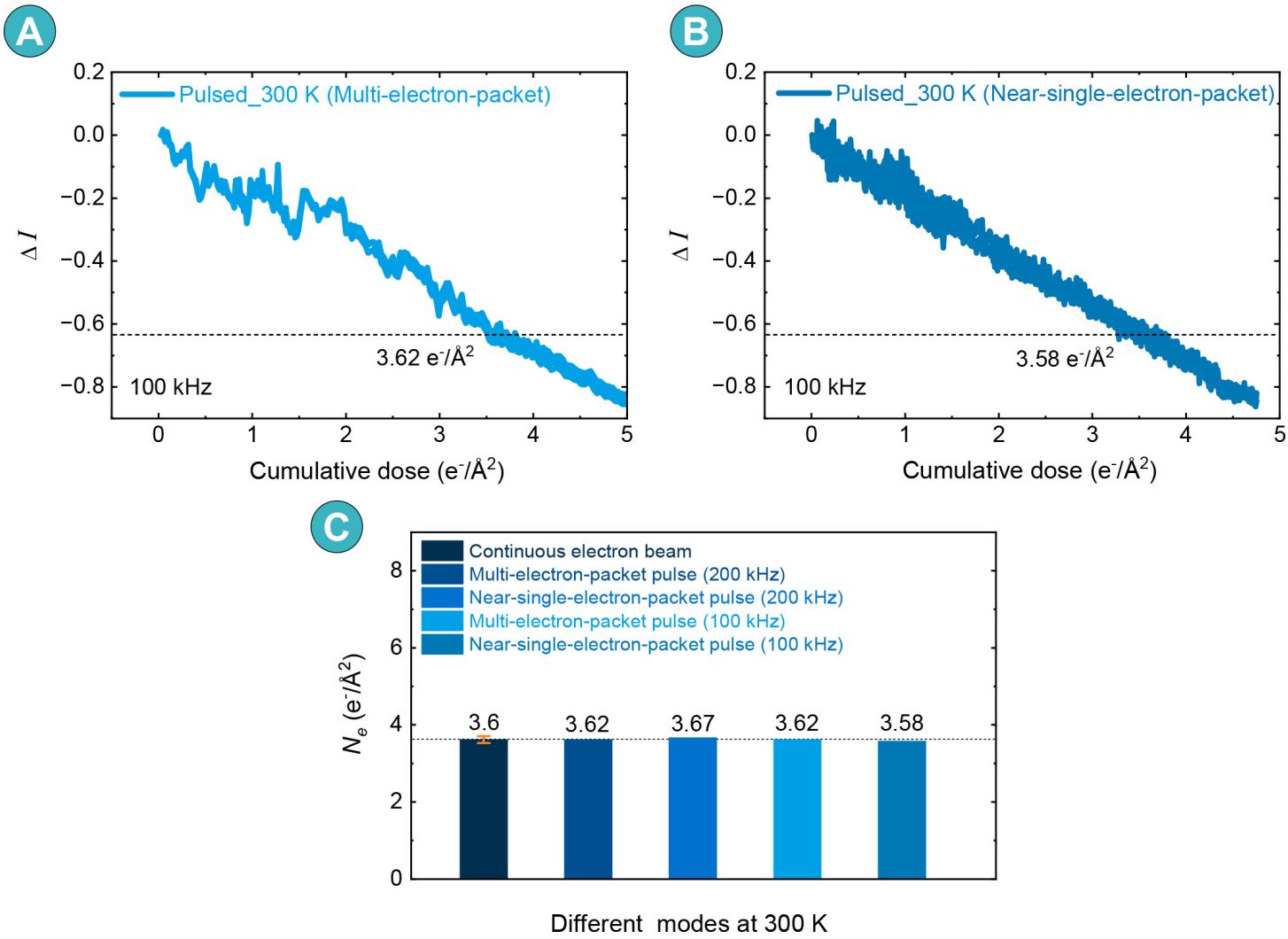

Figure 5. Electron radiation damage of $C_{44}H_{90}$ crystals at 100 kHz laser repetition rate and 300 K (A) The fading curves of diffraction intensity in ultrafast multi-electron-packet pulsed mode, with a N_e value of 3.62 $e^-/Å^2$. (B) The fading curves of diffraction intensity in ultrafast near-single-electron-packet pulsed mode, with a N_e value of 3.58 $e^-/Å^2$. (C) N_e-value statistics of $C_{44}H_{90}$ crystals obtained under different imaging modes and laser repetition rates at 300K.

packet pulsed mode. The N_e values of $C_{44}H_{90}$ crystals at different temperatures (300 K, 200 K and 140 K) and different imaging modes (conventional continuous and multi-electron-packet pulsed modes) were further statistically analyzed (Table 1). At 300 K, the N_e values of $C_{44}H_{90}$ crystals in the modes of conventional continuous and multi-electron-packet pulsed were about 3.6 $e^-/Å^2$ and 3.62 $e^-/Å^2$ respectively; at 200 K, the N_e values were about 5.8 $e^-/Å^2$ and 5.76 $e^-/Å^2$ respectively; at 140 K, the N_e values were about 9.8 $e^-/Å^2$ and 9.62 $e^-/Å^2$ respectively. These findings demonstrate that the multi-electron-packet pulsed imaging mode failed to mitigate electron radiation damage in $C_{44}H_{90}$ samples.

In recent years, it has been reported that the mitigation effect of radiation damage in the ultrafast pulsed mode is related to the number of electrons per pulse (controlled by the laser pulse power) at the laser repetition rate of 200 kHz.[17] Therefore, the diffraction-intensity fading curves of $C_{44}H_{90}$ crystals in the near-single-electron-packet pulsed mode at temperatures of 300 K, 200 K, and 140 K were further measured (in this mode, the number of electrons in each ultrafast electron pulse was less than one (Figure S14), and they were also compared with the fading curves obtained in the conventional continuous electron-beam mode. As shown in Figures 4 and S15, the experimental results showed that, whether at 300 K, 200 K, or 140 K, the diffraction-intensity fading curves of the samples in the near-single-electron-packet pulsed mode were also essentially the same as those obtained in the conventional continuous mode, with completely consistent curve shapes. The N_e values of $C_{44}H_{90}$ crystals in the near-single-electron-packet pulsed mode and the conventional continuous mode at different temperatures were also further statistically analyzed. At 300 K, the N_e values of $C_{44}H_{90}$ crystals in the modes of conventional continuous and near-single-electron-packet pulsed were 3.6 $e^-/Å^2$ and 3.67 $e^-/Å^2$ respectively; at 200 K, the N_e values were 5.8 $e^-/Å^2$ and 5.85 $e^-/Å^2$ respectively; at 140 K, the N_e values were 9.8 $e^-/Å^2$ and 10.04 $e^-/Å^2$ respectively (Table 1). From these data, once again, no mitigation effect of radiation damage was observed to occur. In order to verify the experimental results, we repeated the test more than three times for each mode. These experimental results indicated that the ultrafast pulsed-electron imaging method with time modulation did not seem to mitigate the electron radiation damage in the samples. This finding is consistent with the experimental conclusion of "the independence of radiation damage and N_e values on imaging dose rates" obtained above.

Experimental results at 100 kHz laser repetition rate and room temperature (300 K)

To investigate whether the mitigation effect of radiation damage would be manifested at longer time intervals between pulsed-electron packets (controlled by the laser repetition rates), the diffraction-intensity fading curves of $C_{44}H_{90}$ crystals at 300 K and in pulsed mode were measured again by reducing the laser repetition rate from 200 kHz to 100 kHz. The 100 kHz laser repetition rate corresponds to a temporal interval of 10 μs between successive electron pulses. Compared to the 200 kHz mode, the 100 kHz pulsed mode requires longer data collection time and lower pulsed electron dose rates. As shown in Figures 5 and S16, at 300 K the diffraction-intensity fading curves in multi-electron-packet and near-single-electron-packet pulsed mode at 100 kHz were not different from the fading curves at 200 kHz, and the N_e values were 3.62 $e^-/Å^2$ and 3.58 $e^-/Å^2$, respectively. By statistical anal-

ysis of N_e values obtained in 100 kHz pulsed mode, 200 kHz pulsed mode and conventional continuous mode, it can be found that the N_e values under the three experimental conditions were basically the same (Figure 5C & Table 1). These data showed that modulating the number of electrons in the pulsed-electron packet and the time intervals between the pulsed electron packets did not affect the electron radiation damage in the samples. In other words, time-modulated ultrafast pulsed imaging did not appear to have a mitigation effect on radiation damage.

CONCLUSIONS

In conclusion, we constructed a cryo-UEM device based on an ultrafast laser system and investigated the radiation damage behavior of $C_{44}H_{90}$ crystals under both conventional continuous and ultrafast pulsed electron beams. Experimental results show that the diffraction-intensity fading curves and N_e values of samples are not related to the imaging electron dose rates and do not show any dependence on the dose-rate effect. As the temperature decreased (300 to 140 K), the N_e values of the samples increased by 2.72 times (3.6 to 9.8 $e^-/Å^2$), indicating a cryoprotective effect on radiation damage to the samples. At the constant temperature, the diffraction-intensity fading curves and N_e values of the samples in both multi-electron-packet and near-single-electron-packet pulsed modes are roughly the same as those in conventional continuous mode, even when the results are obtained at different pulsed repetition rates. Our experimental results suggest that the time-modulated pulsed electron beams do not seem to mitigate the electron radiation damage occurred on samples, which is consistent with the views of Glaeser *et al.*[26] Such results indicate that ultrafast pulsed electron imaging with time modulation does not appear to be advantageous in developing into an effective means to overcome the radiation-damage problem of samples in cryo-EM technology. Our findings provide new insights and experimental basis for the sample radiation damage under electron beams, offering guidance and inspiration for elucidating the fundamental principles of radiation damage.

DISCUSSIONS

The dose-rate effect and the mitigation effect of radiation damage in pulsed imaging mode have long been controversial. Here, through long-term and extensive data collection and repeated verification, we have carried out systematic and complete measurements of the diffraction-intensity fading curves of $C_{44}H_{90}$ crystals under different experimental conditions: imaging modes (conventional continuous and ultrafast pulsed), temperatures (140 K to 300 K), imaging dose rates (10^{-5} – 10^{-2} $e^-/Å^2/s$) and pulsed repetition rates (200 kHz and 100 kHz), and obtained the corresponding N_e values (Table 1). The experimental results showed that the electron radiation damage of $C_{44}H_{90}$ crystals did not exhibit a correlation with the imaging electron dose rates, and no mitigation effect of radiation damage was observed in the ultrafast pulsed mode, whether at room temperature or at low temperature. We propose that the observed similarity in electron radiation damage caused by time-modulated ultrafast pulsed electron beams and continuous electron beams may be attributed to the following factors:

(1) A single electron is sufficient to cause irreversible radiation damage to samples, such as bond breakage. In the recent experimental report, Konieczny *et al.* designed a chemical probe for free radical-mediated chain reactions, and found that a Dewar benzene crystal underwent up to 90,000 reactions per incident electron, greatly amplifying the ionization effect in diffraction mode.[54] Moreover, Isaacson *et al.* systematically investigated the interaction between electrons and biomolecules under an electron microscope by characterizing the changes in electron energy loss spectra and electron diffraction patterns, and pointed out that the exponential decrease (just as shown in Figures S17) in the intensities of the energy-loss peak and diffraction peak was consistent with the "single hit" model,[55] *i.e.*, the electron radiation damage was produced by a single energy loss event rather than a succession of events.[56]

(2) The radiation damage of samples is only affected by the energy density, a quantity devoid of time dimension. In many books on X-ray diffraction physics,[57,58] the following statements and related rigorous proofs can be found: the diffraction of crystals arises from scattered photons, and the scattering photons are exactly proportional to the energy density (photons/mm^2), which has no time dimension. This means the crystals are killed by energy density (cumulative dose), rather than time.[59] Such statements are consistent with the experimental results that the dose-rate effect does not exist, *i.e.*, the crystal quality obtained under the same cumulative dose is independent of the speed (electron dose rate) of the applied photons (electrons). On the other hand, as the oldest and most explanatory theory of the radiation-damage curves, the hit theory[55] mentioned in (1) first applied quantum physics ideas to biological problems. It is based on two physical observations and one postulate: I, ionizing radiation transmits the energy in the form of discrete packets. II, the interactions are independent of each other and follow a Poisson distribution. III, if a specified target has received a specified number of hits, the response under investigation will occur. It is clear from these statements that the hit theory, again, incorporates no time dimension.

(3) Just as the dependence of the N_e values on the electron dose rates (dose-rate effect) was not observed in our experimental results, time-dependent cumulative effects, such as thermal effects, may contribute little to the electron radiation damage, implying that even if suitable pulse intervals are provided to allow for structural relaxation and recovery of the sample, the effect on the sample radiation damage is negligible. In a previous study, Thornburg *et al.* observed the warming of samples under a 100 kV electron beam by means of thin film thermocouples, and found that the temperature rise of the samples under "typical" operating conditions was less than 10 K, which was much lower than the empirical values previously reported. Even under extreme beam conditions (100 μA), the temperature of the samples increased by only about 15 K.[60]

(4) If cumulative effects, such as thermal effects, predominate in the radiation damage of saturated hydrocarbon samples, the mitigating effect of radiation damage may be manifested in a pulsed electron beam with suitable time modulation. However, the relaxation and recovery of radiation damage caused by thermal effects could not be accomplished within the time interval of 200 kHz or 100 kHz pulses (based on our experimental results). In addition, as Glaeser said,[26] to a first approximation, the average time between electrons could be arranged to be the same whether the electrons were emitted from a continuous source or a pulsed source. Simply reducing the intensity of the standard continuous source, should provide a long enough pause between inelastic scattering events to allow for the assumed thermal relaxation and recovery. It means that if there is a radiation-damage mitigation effect in the pulsed electron-beam mode, then the mitigation effect should also be observed in the continuous mode with low electron intensity, but this is not the case.

(5) The radiation-damage mechanism of samples under the electron beams is complex and may be affected by the synergistic effect of multiple damage effects. While relevant experimental and theoretical reports have been emerging in recent decades, as Stenn and Bahr lamented in their early reviews,[61] we have to admit that we still know very little about the radiation-damage mechanism of samples due to the extremely complex cascade and synergistic processes involved. Perhaps aside from the longitudinal cascade responses that occur over time, there are also many lateral and cross-propagating cascade responses of radiation damage to the sample at the same time. Given the difficulty of precisely monitoring the events occurring during radiation damage to samples, it still remains uncertain whether the intermittent cessation of the electron beams on the microsecond time scale could lead to the mitigation or disappearance of damage effects such as chemical bond breaking or free radical generation.

It is noteworthy that, with the comprehensive advancement of relevant software and hardware in recent times, the issue of electron radiation damage to samples has emerged as a significant technical bottleneck hindering the further enhancement of material-conformation characterization techniques across various scientific fields, and we hope that more and more groups will join in the systematic study of the electron radiation damage behavior of samples. We believe that it is meaningful to reconsider this topic now, as it concerns the future development of electron imaging technology in new application environments and a new round of "resolution revolution". Here, our research has opened up a new corner for the study of sample radiation damage under electron beams and the integration and proposal of related physical mechanisms. These findings underscore the intricate nature of radiation damage processes and highlight the need for

further exploration of the fundamental principles governing damage mitigation under different experimental conditions.

In future research, leveraging our newly developed cryo-UEM system, we will integrate advanced technical methods to establish a comprehensive TEM imaging framework for observing biomolecular kinetics across femtosecond-to-microsecond timescales. This platform will enable the investigation of potential intermediate transition states in photoexcited photosensitive proteins, providing detailed structural descriptions of ultrafast photochemical events while elucidating their conformational pathways and molecular mechanisms.[62] Unlike X-ray serial crystallography, cryo-UEM has significant advantages including low equipment cost, high popularity, requiring only a small amount of sample, high data collection efficiency, mature data processing technology, and the potential for *in-situ* real-space imaging of amorphous samples, which is expected to advance the entire research field.

REFERENCES

1. Li X., Mooney P., Zheng S., et al. (2013). Electron counting and beam-induced motion correction enable near-atomic-resolution single-particle cryo-EM. *Nat. Methods* **10**:584–590. DOI:10.1038/nmeth.2472
2. Kühlbrandt W. (2014). The resolution revolution. *Science* **343**:1443–1444. DOI:10.1126/science.1251652
3. Tian B., Zhou M., Feng F., et al. (2022). Cryogenic superresolution correlative light and electron microscopy of vitreous sections. *Biophys. Rep.* **8**:193–204. DOI:10.52601/bpr.2022.220005
4. Dubochet J. (2018). On the development of electron cryo-microscopy (nobel lecture). *Angew. Chem. Int. Ed.* **57**:10842–10846. DOI:10.1002/anie.201804280
5. Glaeser R.M., and Taylor K.A. (1978). Radiation damage relative to transmission electron microscopy of biological specimens at low temperature: a review. *J. Microsc.* **112**:127–138. DOI:10.1111/j.1365-2818.1978.tb01160.x
6. Zhang D., Zhu Y., Liu L., et al. (2018). Atomic-resolution transmission electron microscopy of electron beam–sensitive crystalline materials. *Science* **359**:675–679. DOI:10.1126/science.aao0865
7. Cheng Y. (2018). Single-particle cryo-EM—How did it get here and where will it go. *Science* **361**:876–880. DOI:10.1126/science.aat4346
8. Chen Q., Dwyer C., Sheng G., et al. (2020). Imaging beam-sensitive materials by electron microscopy. *Adv. Mater.* **32**:1907619. DOI:10.1002/adma.201907619
9. Jiang N. (2016). Electron beam damage in oxides: a review. *Rep. Prog. Phys.* **79**:016501. DOI:10.1088/0034-4885/79/1/016501
10. Garman E.F., and Weik M. (2023). Radiation damage to biological macromolecules. *Curr. Opin. Struct. Biol.* **82**:102662. DOI:10.1016/j.sbi.2023.102662
11. Egerton R.F. (2012). Mechanisms of radiation damage in beam-sensitive specimens, for TEM accelerating voltages between 10 and 300 kV. *Microsc. Res. Tech.* **75**:1550–1556. DOI:10.1002/jemt.22099
12. Egerton R.F. (2019). Radiation damage to organic and inorganic specimens in the TEM. *Micron* **119**:72–87. DOI:10.1016/j.micron.2019.01.005
13. Glaeser R.M., Mcmullan G., Faruqi A.R., and Henderson R. (2011). Images of paraffin monolayer crystals with perfect contrast: Minimization of beam-induced specimen motion. *Ultramicroscopy* **111**:90–100. DOI:10.1016/j.ultramic.2010.10.010
14. Sun F. (2018). Orienting the future of bio-macromolecular electron microscopy. *Chinese Phys. B* **27**:063601. DOI:10.1088/1674-1056/27/6/063601
15. Baker L.A., and Rubinstein J.L. (2010). Chapter fifteen - radiation damage in electron cryomicroscopy. Jensen G.J. (ed). Methods in enzymology (Academic Press), pp. 371-388. DOI:10.1016/S0076-6879(10)81015-8.
16. Kato K., Miyazaki N., Hamaguchi T., et al. (2021). High-resolution cryo-EM structure of photosystem II reveals damage from high-dose electron beams. *Commun. Biol.* **4**:382. DOI:10.1038/s42003-021-01919-3
17. Vandenbussche E.J., and Flannigan D.J. (2019). Reducing radiation damage in soft matter with femtosecond-timed single-electron packets. *Nano Lett.* **19**:6687–6694. DOI:10.1021/acs.nanolett.9b03074
18. Xue H., Zhang M., Liu J., et al. (2022). Cryo-electron tomography related radiation-damage parameters for individual-molecule 3D structure determination. *Front. Chem.* **10**:889203. DOI:10.3389/fchem.2022.889203
19. Bonham R.A., and Kennerly R.E. (1978). Pulsed electron beams to reduce radiation damage. *Ann. N. Y. Acad. Sci.* **306**:85–94. DOI:10.1111/j.1749-6632.1978.tb25641.x
20. Glaeser R.M. (2025). Commonsense and common nonsense opinions: prospects for further reducing beam damage in electron microscopy of radiation-sensitive specimens. *Ultramicroscopy* **271**:114118. DOI:10.1016/j.ultramic.2025.114118
21. Grubb D.T. (1974). Radiation damage and electron microscopy of organic polymers. *J. Mater. Sci.* **9**:1715–1736. DOI:10.1007/BF00540772
22. Flannigan D.J., and Vandenbussche E.J. (2023). Pulsed-beam transmission electron microscopy and radiation damage. *Micron* **172**:103501. DOI:10.1016/j.micron.2023.103501
23. Flannigan D.J., Curtis W.A., Vandenbussche E.J., and Zhang Y. (2022). Low repetition-rate, high-resolution femtosecond transmission electron microscopy. *J. Chem. Phys.* **157**:180903. DOI:10.1063/5.0128109
24. Kisielowski C., Specht P., Freitag B., et al. (2019). Discovering hidden material properties of $MgCl_2$ at atomic resolution with structured temporal electron illumination of picosecond time resolution. *Adv. Funct. Mater.* **29**:1807818. DOI:10.1002/adfm.201807818
25. Kisielowski C., Specht P., Rozeveld S., et al. (2022). Exploring functional materials by understanding beam-sample interactions. *Adv. Funct. Mater.* **32**:2201112. DOI:10.1002/adfm.202201112
26. Glaeser R.M. (2008). Retrospective: Radiation damage and its associated "Information Limitations". *J. Struct. Biol.* **163**:271–276. DOI:10.1016/j.jsb.2008.06.001
27. Glaeser R.M. (1971). Limitations to significant information in biological electron microscopy as a result of radiation damage. *J. Ultrastruct. Res.* **36**:466–482. DOI:10.1016/S0022-5320(71)80118-1
28. Taylor K.A., and Glaeser R.M. (1976). Electron microscopy of frozen hydrated biological specimens. *J. Ultrastruct. Res.* **55**:448–456. DOI:10.1016/S0022-5320(76)80099-8
29. Glaeser R.M. (1979). Prospects for extending the resolution limit of the electron microscope. *J. Microsc.* **117**:77–91. DOI:10.1111/j.1365-2818.1979.tb00232.x
30. Jeng T.-W., and Chiu W. (1984). Quantitative assessment of radiation damage in a thin protein crystal. *J. Microsc.* **136**:35–44. DOI:10.1111/j.1365-2818.1984.tb02544.x
31. Sliz P., Harrison S.C., and Rosenbaum G. (2003). How does radiation damage in protein crystals depend on X-ray dose. *Structure* **11**:13–19. DOI:10.1016/S0969-2126(02)00910-3
32. Nannenga B.L., Bu G., and Shi D. (2018). The evolution and the advantages of MicroED. *Front. Mol. Biosci.* **5**:DOI:10.3389/fmolb.2018.00114
33. Chen J.Z., Sachse C., Xu C., et al. (2008). A dose-rate effect in single-particle electron microscopy. *J. Struct. Biol.* **161**:92–100. DOI:10.1016/j.jsb.2007.09.017
34. Jiang N., and Spence J.C.H. (2012). On the dose-rate threshold of beam damage in TEM. *Ultramicroscopy* **113**:77–82. DOI:10.1016/j.ultramic.2011.11.016
35. Matsuya Y., Mcmahon S.J., Tsutsumi K., et al. (2018). Investigation of dose-rate effects and cell-cycle distribution under protracted exposure to ionizing radiation for various dose-rates. *Sci . Rep.* **8**:8287. DOI:10.1038/s41598-018-26556-5
36. Dubochet J., Adrian M., Chang J.-J., et al. (1988). Cryo-electron microscopy of vitrified specimens. *Q . Rev. Biophys.* **21**:129–228. DOI:10.1017/S0033583500004297
37. Lobastov V.A., Weissenrieder J., Tang J., and Zewail A.H. (2007). Ultrafast electron microscopy (UEM): Four-dimensional imaging and diffraction of nanostructures during phase transitions. *Nano Lett.* **7**:2552–2558. DOI:10.1021/nl071341e
38. Shorokhov D., and Zewail A.H. (2016). Perspective: 4D ultrafast electron microscopy—Evolutions and revolutions. *J. Chem. Phys.* **144**:080901. DOI:10.1063/1.4941375
39. Kim Y.-J., Park W.-W., Nho H.-W., and Kwon O.-H. (2024). High-resolution correlative imaging in ultrafast electron microscopy. *Adv. Phys-X* **9**:2316710. DOI:10.1080/23746149.2024.2316710
40. Nabben D., Kuttruff J., Stolz L., et al. (2023). Attosecond electron microscopy of sub-cycle optical dynamics. *Nature* **619**:63–67. DOI:10.1038/s41586-023-06074-9
41. Vanacore G.M., Fitzpatrick A.W.P., and Zewail A.H. (2016). Four-dimensional electron microscopy: Ultrafast imaging, diffraction and spectroscopy in materials science and biology. *Nano Today* **11**:228–249. DOI:10.1016/j.nantod.2016.04.009
42. Armstrong M.R., Boyden K., Browning N.D., et al. (2007). Practical considerations for high spatial and temporal resolution dynamic transmission electron microscopy. *Ultramicroscopy* **107**:356–367. DOI:10.1016/j.ultramic.2006.09.005
43. Kuwahara M., and Agemura T. (2023). Temporal resolution in transmission electron microscopy using a photoemission electron source. *Microscopy* **72**:97–110. DOI:10.1093/jmicro/dfac069
44. Du D.X., Simjanoska M., and Fitzpatrick A.W.P. (2023). Four-dimensional microED of conformational dynamics in protein microcrystals on the femto-to-microsecond timescales. *J. Struct. Biol.* **215**:107941. DOI:10.1016/j.jsb.2023.107941
45. Peet M.J., Henderson R., and Russo C.J. (2019). The energy dependence of contrast and damage in electron cryomicroscopy of biological molecules. *Ultramicroscopy* **203**:125–131. DOI:10.1016/j.ultramic.2019.02.007
46. Naydenova K., Kamegawa A., Peet M.J., et al. (2022). On the reduction in the effects of radiation damage to two-dimensional crystals of organic and biological molecules at liquid-helium temperature. *Ultramicroscopy* **237**:113512. DOI:10.1016/j.ultramic.2022.113512
47. Cao G., Sun S., Li Z., et al. (2015). Clocking the anisotropic lattice dynamics of multi-walled carbon nanotubes by four-dimensional ultrafast transmission electron microscopy. *Sci. Rep.* **5**:8404. DOI:10.1038/srep08404
48. Yan R., Edwards T.J., Pankratz L.M., et al. (2015). Simultaneous determination of sample thickness, tilt, and electron mean free path using tomographic tilt images based on Beer–Lambert law. *J. Struct. Biol.* **192**:287–296. DOI:10.1016/j.jsb.2015.09.019
49. Baker L.A., Smith E.A., Bueler S.A., and Rubinstein J.L. (2010). The resolution dependence of optimal exposures in liquid nitrogen temperature electron cryomicroscopy of catalase crystals. *J. Struct. Biol.* **169**:431–437. DOI:10.1016/j.jsb.2009.11.014
50. Unwin P.N.T., and Henderson R. (1975). Molecular structure determination by electron microscopy of unstained crystalline specimens. *J. Mol. Biol.* **94**:425–440. DOI:10.1016/0022-2836(75)90212-0
51. Hayward S.B., and Glaeser R.M. (1979). Radiation damage of purple membrane at

low temperature. *Ultramicroscopy* **4**:201–210. DOI:10.1016/S0304-3991(79)90211-0
52. Siegel G. (1972). The influence of very low temperature on the radiation damage of organic crystals irradiated by 100 keV-electrons. *Z. Naturforsch.* **27**:325–332. DOI:10.1515/zna-1972-0219
53. Li Y., Kang D.-D., Dai J.-Y., and Wang L.-W. (2024). The cage effect of electron beam irradiation damage in cryo-electron microscopy. *npj Comput. Mater.* **10**:115. DOI:10.1038/s41524-024-01299-2
54. Konieczny K.A., Paul I., Rodriguez J.A., and Garcia-Garibay M.A. (2024). From beam damage to massive reaction amplification under the electron microscope: an ionization-induced chain reaction in crystals of a dewar benzene. *ACS Cent. Sci.* DOI:10.1021/acscentsci.4c01429
55. Dertinger H., and Jung H. (1970). The hit theory. Dertinger H., and Jung H. (ed). Molecular radiation biology (Springer US), pp. 12-23. DOI:10.1007/978-1-4684-6247-0_2.
56. Isaacson M., Johnson D., and Crewe A.V. (1973). Electron beam excitation and damage of biological molecules; Its implications for specimen damage in electron microscopy. *Radiat. Res.* **55**:205–224. DOI:10.2307/3573678
57. Drenth J. (1999). The theory of X-ray diffraction by a crystal. Drenth J. (ed). Principles of protein X-ray crystallography (Springer New York), pp. 70-116. DOI:10.1007/978-1-4757-3092-0_4
58. Woolfson M.M. (1997). An introduction to X-ray crystallography (Cambridge University Press). DOI:10.1017/CBO9780511622557
59. Holton J. (2009). A beginner's guide to radiation damage. *J. Synchrotron Radiat.* **16**:133–142. DOI:10.1107/S0909049509004361
60. Thornburg D.D., and Wayman C.M. (1973). Specimen temperature increases during transmission electron microscopy. *phys. stat. sol. (a)* **15**:449–453. DOI:10.1002/pssa.2210150209
61. Stenn K., and Bahr G.F. (1970). Specimen damage caused by the beam of the transmission electron microscope, a correlative reconsideration. *J. Ultrastruct. Res.* **31**:526–550. DOI:10.1016/S0022-5320(70)90167-X
62. Li Z., and Peng G. (2022). Spatial transcriptomics: new dimension of understanding biological complexity. *Biophys. Rep.* **8**:119–135. DOI:10.52601/bpr.2021.210037

FUNDING AND ACKNOWLEDGMENTS

We thank Yujia Zhai for helpful discussions, Zhongwen Li and Chaoxiang Chen for modifying the cryo-UEM. The study is funded by the National Key Research and Development Program (2021YFA1301500, 2019YFA0904101), National Natural Science Foundation of China (31925026, 32400996, T2495223), the Strategic Priority Research Program of the Chinese Academy of Sciences (XDB37040102), Beijing Natural Science Foundation (JQ24056), Postdoctoral Fellowship Program of CPSF (GZC20232900), Chinese Academy of Sciences Research Instruments and Equipment Development Program (ZDKYYQ20170002). The funders had no role in study design, data collection and analysis, decision to publish or preparation of the manuscript.

AUTHOR CONTRIBUTIONS

Fei Sun, Jianqi Li and Huaixin Yang conceived the research; Yimin Zhao, Chen Qi, Chunhui Zhu and Yun Zhu performed the experiments; Yongzhao Zhang, Tongnian Gu, Huanfang Tian, Wentao Wang and Siyuan Huang discussed and solved the problems encountered in the experiment; Fei Sun, Jianqi Li and Huaixin Yang directed the research; Yimin Zhao, Chen Qi, Yun Zhu and Fei Sun analyzed the data; Yimin Zhao and Fei Sun wrote the paper. All authors contributed to the manuscript and approved the final version.

DECLARATION OF INTERESTS

The authors declare no competing interests.

ETHICAL STATEMENT AND PATIENT CONSENT

Not applicable.

DATA AND CODE AVAILABILITY

Data generated or analyzed during this study are included in the published article and its Supplemental Information. Any additional information required to reanalyze the data reported in this paper is available from the lead contact upon request.

SUPPLEMENTAL INFORMATION

It can be found online at https://doi.org/10.59717/j.xinn-life.2025.100145

LEAD CONTACT WEBSITE

Fei Sun: http://www.ibp.cas.cn/feilab/home/